ORIGINAL PAPER

Effect of Preparation Conditions on Precipitated Iron-Based Catalysts for High-Temperature Fischer–Tropsch Synthesis of Light Olefins

Yi Yang[1] · Haitao Zhang[1] · Hongfang Ma[1] · Weixin Qian[1] · Qiwen Sun[2] · Weiyong Ying[1]

Abstract

A series of catalysts prepared by precipitation method were used to investigate the effects of preparation conditions on iron-based catalysts for high-temperature Fischer–Tropsch synthesis (HTFT) of light olefins. In this study, we varied the titration methods (forward precipitation, concurrent precipitation, and reverse precipitation), iron precursors [$Fe(NO_3)_3$, $Fe_2(SO_4)_3$, and $FeCl_3$], precipitants (ammonium carbonate, sodium carbonate, ammonia solution, sodium hydroxide, and potassium hydroxide), precipitation pH values (pH = 6.0, 7.0, 8.0, and 9.0), precipitation temperature (temperature = 25 °C, 45 °C, 65 °C, 75 °C, and 85 °C) and incorporation manners of Mn promoter (precipitation and incipient wetness impregnation method). It was demonstrated that different preparation conditions affect the BET specific surface area, pore structure, the morphology and dispersion of the catalyst, grain size, reduction ability, and CO adsorption ability of the catalyst, which in turn affect the activity of the catalyst and the production of light olefins during the HTFT. The results showed that the iron-based catalysts with the optimum catalytic performance and production of light olefins were prepared under the following conditions: ammonium carbonate as the precipitant and ferric trichloride as the iron precursor by concurrent precipitation method at pH 8.0 and 65 °C, followed by the introduction of Mn promoter by precipitation method. Catalysts were characterized by Ar adsorption–desorption, X-ray diffraction (XRD), scanning electron microscopy (SEM), H_2 temperature-programmed reduction (H_2-TPR), and CO-temperature-programmed desorption (CO-TPD).

Keywords Fischer–Tropsch synthesis · Light olefins · Preparation conditions · Iron-based catalyst

1 Introduction

Light olefins ($C_2^=$–$C_4^=$) are the most basic organic chemical feedstock used in the production of petroleum and chemical industries. Light olefins are used in the production of many chemical products, such as polymers, pharmaceuticals, cosmetics, and detergents. The direct production of light olefins from coal via syngas by Fischer–Tropsch is an important non-petroleum route [1, 2]. Compared to low-temperature Fischer–Tropsch synthesis, high-temperature

Fischer–Tropsch (HTFT) synthesis is more suitable for the production of short-chain hydrocarbons than low-temperature Fischer–Tropsch synthesis. Similarly, iron-based catalysts are more likely to shift the hydrocarbon distribution toward lower molecular mass hydrocarbons than cobalt-based catalysts [3, 4].

In Fischer–Tropsch synthesis, the preparation condition has an important influence on the performance of iron catalysts. FTS is a structure-sensitive reaction, and changes in the properties of the catalyst itself can affect the performance of the catalyst [3]. Furthermore, different preparation conditions affect the specific surface area, pore structure, the morphology and dispersion of the catalyst, grain size, reduction ability, and CO adsorption ability of the catalyst, which in turn affect the activity of the catalyst and the production of light olefins during the HTFT [5–8]. Therefore, it is necessary to select a suitable preparation condition for the preparation of iron-based catalysts for FTS. Torres Galvis et al. [9] examined the effect of different iron precursors (iron nitrate and ferric ammonium citrate) on iron catalysts

✉ Weixin Qian
  wxqian@ecust.edu.cn

[1] Engineering Research Center of Large Scale Reactor Engineering and Technology, Ministry of Education, State Key Laboratory of Chemical Engineering, School of Chemical Engineering, East China University of Science and Technology, Shanghai 200237, China

[2] State Key Laboratory of Coal Liquefaction and Coal Chemical Technology, Shanghai 201203, China

for light olefins. The results showed that the catalysts prepared with ferric ammonium citrate exhibited higher catalytic activity and lower carbon deposition rates compared to those prepared with iron nitrate. They attribute the difference in catalytic performance to the more uniform particles of the iron catalysts prepared with ferric ammonium citrate. Wei et al. [10] prepared graphene oxide loaded iron catalysts using three different iron precursors (ferrous acetate, iron oxalate, and iron nitrate), respectively, and found that the iron catalyst prepared from iron oxalate exhibited higher FTS activity and C_5^+ selectivity due to the advantages of small and uniform particles size, which promoted the reduction and carbonation of the catalyst. Moreover, Motjope et al. [7] prepared three precipitated iron-based catalysts of the same composition using sodium carbonate, potassium carbonate, and ammonia as precipitants. It was shown that the larger pore volume and pore size observed for the catalysts prepared from sodium and potassium carbonate could be attributed to the CO_2 formed during the precipitation process, the catalyst prepared from ammonia solution exhibited the highest CO conversion, but the CO conversion showed a significant decrease after 15 h, while the catalyst prepared from sodium carbonate exhibited higher stability after 15 h. Zhao et al. [6] explored the effect of precipitants (sodium carbonate, potassium carbonate, ammonium carbonate, and urea) on the catalytic performance of FeZn catalysts. The FeZn catalysts prepared with alkali metal carbonates (sodium carbonate, potassium carbonate) exhibited better catalytic performance because the residual Na^+ or K^+ could promote the conversion of CO to heavy hydrocarbons, and improve the O/P ratio. In contrast, the catalysts prepared using ammonium carbonate and urea as precipitants produced more alkanes in the products and showed low selectivity for light olefins. Furthermore, Mirzaei et al. [11] prepared a series of FeMn catalysts using the precipitation method at pH values between 6.3 and 10.3. The results showed that the highest catalytic activity was achieved at pH = 8.3. Feyzi et al. [12] prepared a series of FeCo catalysts using a precipitation method at pH values between 6.0 and 9.0. The results showed that the catalysts displayed high CO conversion and light olefins selectivity at pH = 7.5. Mirzaei et al. [11] investigated the effect of precipitation temperature in the range of 40–80 °C on FeMn catalysts prepared by precipitation, and the results showed that 70 °C was the optimum precipitation temperature. Additionally, Mai et al. [8] prepared iron-based catalysts for FTS by impregnation and precipitation methods, respectively, and showed that the catalysts prepared by the precipitation method exhibited higher CO conversion and light olefins selectivity. Wu et al. [13] discussed that Mn could enhance dissociative adsorption of CO, thereby promoting the selectivity to $C_2^=–C_4^=$.

Although the preparation condition variables of iron-based catalysts in FTS have been widely studied, there

is a lack of comprehensive and systematic reports on the preparation conditions of iron-based catalysts in HTFT, and the effects of the preparation condition variables of pure Fe-based catalysts without any promoters have been rarely reported. Herein, the objective of this research work was to comprehensively and systematically investigate the effects of a range of preparation condition variables on precipitated iron-based catalysts for HTFT of light olefins, including the titration methods (forward precipitation, concurrent precipitation, and reverse precipitation), iron precursors [$Fe(NO_3)_3$, $Fe_2(SO_4)_3$, and $FeCl_3$], precipitants (ammonium carbonate, sodium carbonate, ammonia solution, sodium hydroxide, and potassium hydroxide), precipitation pH values (pH = 6.0, 7.0, 8.0, and 9.0), precipitation temperature (temperature = 25 °C, 45 °C, 65 °C, 75 °C, and 85 °C) and incorporation manners of Mn promoter (precipitation and incipient wetness impregnation method). All catalysts were characterized by Ar adsorption–desorption, scanning electron microscopy (SEM), X-ray diffraction (XRD), H_2 temperature-programmed reduction (H_2-TPR), and CO-temperature-programmed desorption (CO-TPD). The study compares the catalytic activity under different preparation conditions, which provides an idea for the design of HTFT precipitated iron-based catalysts.

2 Experimental Section

2.1 Preparation of Catalysts

All iron-based catalysts were prepared by concurrent precipitation method except Sect. 3.1. The iron precursor was a solution of $Fe(NO_3)_3 \cdot 9H_2O$ (99 wt%, Macklin). The precipitant was sodium carbonate (> 99.99 wt%, Macklin). The iron precursor solution and sodium carbonate solution were introduced drop by drop into a beaker at the same time at 25 °C, stirring continuously. The pH of the mixed solution was controlled at 8.0 ± 0.1 and the stirring was carried out for 1 h. The mix solution was aged for 4 h, washed with deionized water, dried at 110 °C for 12 h, and finally calcined at 500 °C for 4 h.

In order to compare the effect of titration methods, forward precipitation, concurrent precipitation, and reverse precipitation were used to prepare catalysts. Forward precipitation was the addition of precipitant to the iron precursor solution. Reverse precipitation was the addition of iron precursor solution to the precipitant. The catalysts with different titration methods (forward precipitation, concurrent precipitation, and reverse precipitation) were labeled Fe–F, Fe–C, and Fe–R, respectively.

To compare the effect of iron precursors, $Fe(NO_3)_3$ (99 wt%, Macklin), $Fe_2(SO_4)_3$ (99 wt%, Macklin), and $FeCl_3$ (99 wt%, Macklin) were used as different iron precursors with

sodium carbonate as precipitant. The catalysts with different iron precursors (Fe(NO$_3$)$_3$, Fe$_2$(SO$_4$)$_3$, and FeCl$_3$) were labeled Fe–N, Fe–S, and Fe–Cl, respectively.

To compare the effect of different precipitants, ammonium carbonate (99.99 wt%, Macklin), sodium carbonate (99.99 wt%, Macklin), ammonia solution (25–28%, AR, Macklin), sodium hydroxide (98 wt%, Macklin), and potassium hydroxide (99 wt%, Macklin) were used as different precipitants. The catalysts with different precipitants (ammonium carbonate, sodium carbonate, ammonia solution, sodium hydroxide, and potassium hydroxide) were labeled Fe-AC, Fe-SC, Fe-AH, Fe-SH, and Fe-PH, respectively.

The catalysts with ammonium carbonate as precipitant with different precipitation pH values (pH = 6.0, 7.0, 8.0, and 9.0) were labeled Fe-pH6.0, Fe-pH7.0, Fe-pH8.0, and Fe-pH9.0, respectively.

The catalysts with ammonium carbonate as precipitant with different temperatures of precipitation (temperature = 25 °C, 45 °C, 65 °C, 75 °C, and 85 °C) were labeled Fe-Tem25, Fe-Tem45, Fe-Tem65, Fe-Tem75, and Fe-Tem85, respectively.

Moreover, to compare the effect of different incorporation manners of Mn promoter, the precipitation method and incipient wetness impregnation method were used to prepare catalysts. FeMn catalyst was prepared in the same method as Fe-Tem65 catalyst with the addition of Mn(NO$_3$)$_2$ (50 wt% aq. AR, Aladdin) to the metal source. The precipitation catalyst with molar compositions as 100Fe/5Mn was labeled FeMn. Furthermore, Mn/Fe catalyst was prepared by incipient wetness impregnation methods. The Fe-Tem65 precursor was impregnated with Mn(NO$_3$)$_2$ solutions of the required concentration. Subsequently, the sample was aged at room temperature for 24 h, dried at 110 °C for 12 h, and finally calcined at 500 °C for 4 h. The impregnation catalyst with molar compositions as 100 Fe/5 Mn was labeled Mn/Fe. And the catalyst without Mn promoter prepared in the same way as Fe-Tem65 was labeled Fe.

2.2 Catalyst Characterization

The compositions of samples were determined using inductively coupled plasma atomic emission spectroscopy using Agilent 725ES equipment (ICP-AES).

Ar physical adsorption–desorption isotherms acquired with a Micrometric ASAP 2020 at 87 K were used to investigate the textural features of fresh catalysts. The Brunauer–Emmett–Teller technique was used to calculate the specific surface area. Barrett-Joyner-Halenda was used to calculate the pore volume and average pore diameter.

A powder X-ray diffractometer (D/MAX2550 VB/PC) employing Cu Kα radiation (λ = 0.154 nm, 40 kV, and 100 mA) was used to determine the crystalline structure of the samples. The samples were measured in a scanning rate of 6° min^{-1} and a 2θ range of 10°–80°.

SEM images were taken with an FEI Inspect F50 microscope operated at 10 kV accelerating voltage.

A Micromeritics AutoChemII 2920 device was used to perform an H$_2$ temperature-programmed reduction (H$_2$-TPR) test. The catalyst (50 mg) was purified at 350 °C for 30 min under He flow before each measurement. The system was then cooled to 60 °C. Following that, at a flow rate of 50 mL/min, the sample was subjected to a mixture of 10% H$_2$/90% Ar (v/v). The reduction temperature was increased from 60 to 800 °C at a rate of 10 °C/min during this operation.

CO-TPD studies were carried out using a Micromeritics AutoChemII 2920 device. The sample (200 mg) was reduced at 350 °C for 10 h with H$_2$ flow before being cooled to 60 °C with He gas flow. After that, the sample was exposed to a CO flow for 30 min. The temperature was then raised at a rate of 10 °C/min from 60 to 800 °C, with the outflow measured using a thermal conductivity detector (TCD).

2.3 Catalyst Testing and Product Analysis

The HTFT reaction was tested in a tubular fixed-bed reactor (ID = 10 mm). Generally, 0.3 g prepared catalyst (particle size: 40–60 mesh) with 0.6 g of quartz grains of the same particle size was loaded into a stainless-steel reactor. Before measurement, catalysts were reduced at 350 °C for 10 h in H$_2$ flowing [6000 mL/(h g$_{Cat}$)]. The HTFT reaction was carried out at 320 °C, 1.0 MPa, H$_2$/CO = 2 mol/mol, and 12,000 mL/(h g$_{Cat}$). After the HTFT reaction performance, the tail gases CO, H$_2$, CH$_4$, and others were detected using an Agilent 7890A online GC with three types of columns (HP-AL/S; HayeSep Q; Sieve 5A). The oils and waxes were detected on an offline Agilent 7890A with a column (HP-5), while the water was detected on an offline Agilent 7890A with a column (DB-WAX).

Equations (1)–(3) were used to calculate CO conversion (X_{CO}, %), CO$_2$ selectivity (S_{CO2}, %), and hydrocarbon distribution ($S_{C_iH_j}$, %) for each hydrocarbon.

$$X_{CO}(\%) = \frac{N_{in, CO} - N_{out, CO}}{N_{in, CO}} \times 100\% \tag{1}$$

$$S_{CO_2}(\%) = \frac{N_{out, CO_2}}{N_{in, CO} - N_{out, CO}} \times 100\% \tag{2}$$

$$S_{C_iH_j}(\%) = \frac{iN_{out, C_iH_j}}{\sum_{i=1}^{n} iN_{out, C_iH_j}} \times 100\% \tag{3}$$

where N_{in} and N_{out} are the inlet and outlet gas molar flow rate, respectively, and C_iH_j is the carbon atom count.

Table 1 Ar-physisorption results of the fresh catalysts

Catalyst	Na$^+$ (wt%)^a	S_{BET} (m^2/g)	V_P (cm^3/g)	D_P (nm)	d_{Fe2O3}^{b} (nm)
Fe–F	0.28	41.4	0.19	13.2	13.0
Fe–C	0.20	31.2	0.25	22.2	19.1
Fe–R	0.26	30.0	0.27	25.5	18.6

^{a}Determined by ICP-AES

^{b}Calculated by Scherrer equation according to XRD

# 3 Results and Discussion

3.1 Effect of Titration Methods on Catalysts

The textural properties of precipitated iron-based catalysts with different titration methods (forward precipitation, concurrent precipitation, and reverse precipitation) are shown in Table 1.

Based on the ICP-AES results, the residual Na$^+$ contents of these three samples are similar (0.20–0.28 wt%). Fig. S1 shows the adsorption–desorption isotherms of the fresh catalysts with different titration methods. As shown in Fig. S1, this is a type IV isotherm with a typical H1 hysteresis loop, which indicates that the pore structure of the sample is mainly a mesoporous structure made of nanoparticles connected [14]. During Fischer–Tropsch synthesis, these characteristics help to reduce the mass transfer resistance and shorten the feed gas residence time, thus promoting the formation of low carbon hydrocarbons and inhibiting the formation of high carbon hydrocarbons [15, 16]. As can be seen from Table 1, the Fe–F catalyst has the largest BET specific surface area, followed by the Fe–C catalyst, and the smallest is the Fe–R catalyst. Additionally, the Fe–R catalyst has the largest pore volume and average pore size, followed by the Fe–C catalyst, and the smallest is the Fe–F catalyst.

The XRD patterns of precipitated iron-based catalysts with different titration methods are shown in Fig. 1. According to JCPDS#87-1164, all three catalysts show the same α-Fe$_2$O$_3$ characteristic diffraction peaks at the same locations. And the diffraction peaks of α-Fe$_2$O$_3$ show a significant difference in intensity, indicating that the average crystallite size of α-Fe$_2$O$_3$ in the catalyst is influenced by titration methods. Based on the XRD full spectrum, the average crystallite size of α-Fe$_2$O$_3$ is calculated using the Scherrer equation, and the results are shown in Table 1. Fe–F catalyst prepared by forward precipitation exhibits the smallest average crystallite size, while Fe–C catalysts prepared by concurrent precipitation exhibited the largest average crystallite size.

The SEM pictures of precipitated iron-based catalysts with forward precipitation and concurrent precipitation are shown in Fig. 2. Two catalysts consist of sphere-like
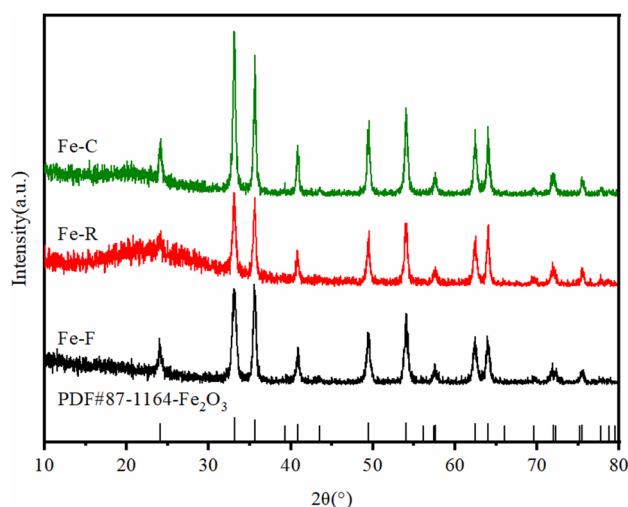
Fig. 1 XRD patterns of fresh catalysts

nanoparticles. And the catalysts with mesopores and inter-granular pores that are in good agreement with the Ar physisorption result. In addition, Fe–F catalyst exhibits significant aggregation of iron nanoparticles, while Fe–C catalyst exhibits good dispersion of iron nanoparticles. The pH value of the metal nitrate solution is about 3 and the pH value of the precipitant solution is about 12. When Fe–F catalyst is prepared by forward precipitation, the precipitate is rapidly dissolved with precipitant drop addition. And as the precipitant continues to be added dropwise, the solution changes from acidic to neutral, and then a large amount of precipitate is suddenly formed. The crystal nuclei are formed rapidly within a short period and cannot grow sufficiently, resulting in the small size of iron nanoparticles and slight aggregation to some extent. However, Fe–C catalyst is prepared by concurrent precipitation, in which the metal nitrate solution and the precipitant are added dropwise to the beaker at the same time, and the titration rate is controlled to keep the solution in the beaker at pH = 8.0, Thus, the precipitate is formed gradually as the titration proceeds, and the precipitate is well dispersed by vigorous stirring, resulting in good dispersion of the iron precursor and thus the final iron nanoparticles. Because the crystal nuclei can grow sufficiently by concurrent precipitation, the Fe–C nanoparticles formed by concurrent precipitation are slightly larger compared to those formed by forward precipitation, which is consistent with the XRD results.

The H$_2$-TPR profiles of precipitated iron-based catalysts with different titration methods are shown in Fig. 3. As can be seen in Fig. 3, all three catalysts exhibit two distinct reduction stages at low and high temperatures region. The reduction peak in the low-temperature region (250–300 °C) is considered as the conversion of α-Fe$_2$O$_3 \rightarrow$ Fe$_3$O$_4$, and the reduction peak in the high-temperature region (350–700 °C)

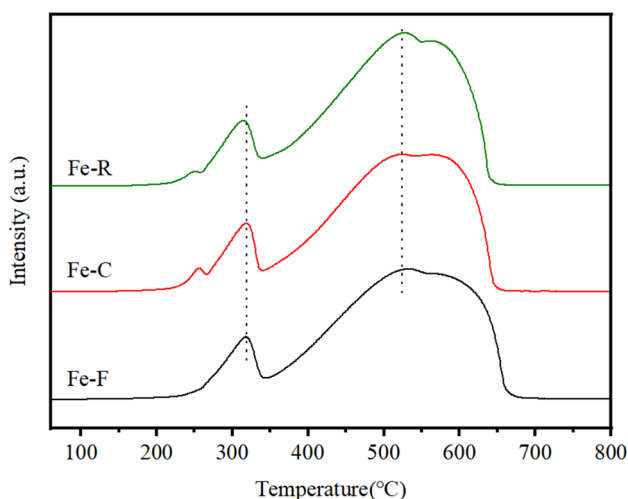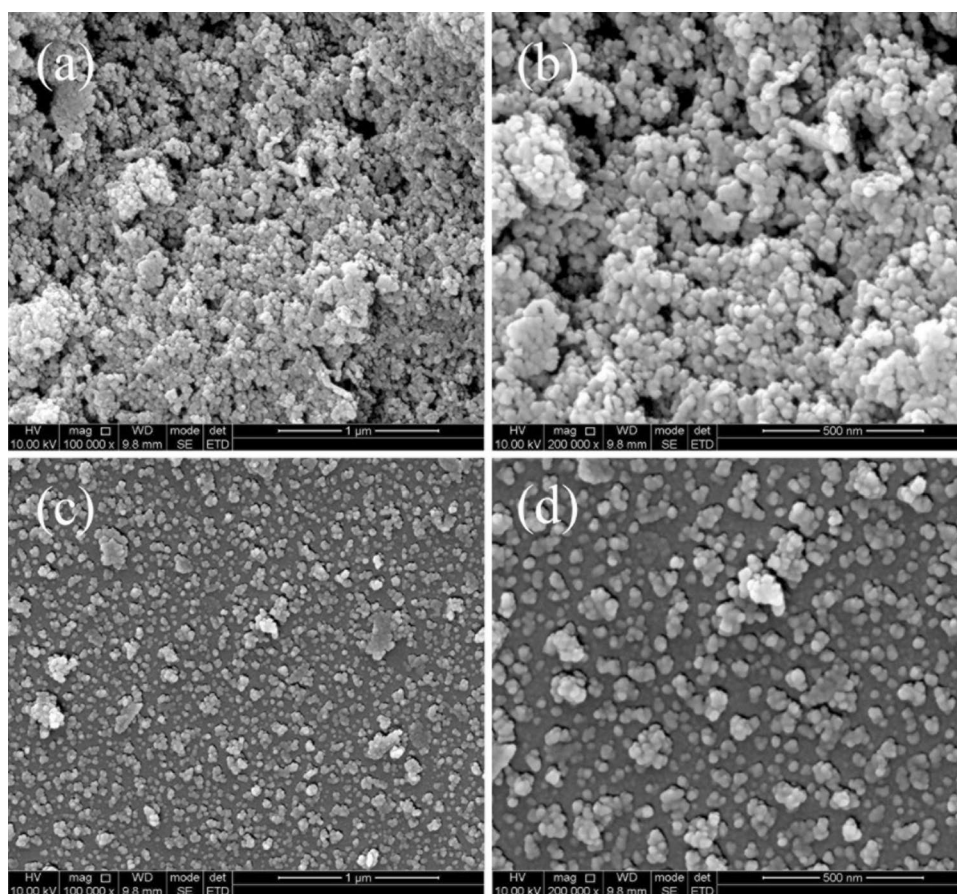**Fig. 2** SEM images of fresh catalysts **a**, **b** Fe–F, **c**, **d** Fe–C

Fig. 3 H$_2$-TPR profiles of the fresh catalysts

is attributed to the conversion of Fe$_3$O$_4 \rightarrow$ FeO $\rightarrow \alpha$-Fe [17, 18]. On the one hand, the low temperature reduction peak temperature of Fe–R catalyst is lower than that of Fe–C and Fe–F catalysts. On the other hand, the order of peak widths in the high temperature reduction stage is: Fe–F > Fe–C > Fe–R. Therefore, the order of the ease of reduction of precipitated iron catalysts is: Fe–R > Fe–C > Fe–F, and Fe–F has the largest peak width in the high temperature reduction stage, implying that the iron phase is more difficult to be reduced.

The CO-TPD patterns of the reduced catalysts with different titration methods are shown in Fig. 4. The first desorption peak at a temperature around 100 °C is attributed to CO molecular adsorption, and the second desorption peak at a temperature between 300 and 650 °C is attributed to CO dissociative adsorption [19, 20]. On the one hand, the peak areas of CO molecule desorption for Fe–C and Fe–R catalysts are significantly larger than that for Fe–F catalyst. On the other hand, the CO dissociation desorption peaks move toward the high temperature. This result indicates that concurrent precipitation and reverse precipitation promote CO molecular adsorption and CO dissociative adsorption.

The effects of different titration methods (forward precipitation, concurrent precipitation, and reverse precipitation) on the HTFT synthesis performance are investigated, and the HTFT synthesis activities and hydrocarbon distributions are shown in Table 2. By comparing the CO conversion of catalysts, it can be found that the order of CO conversion is: Fe–C (90.8%) > Fe–R (86.9%) > Fe–F (55.5%). According
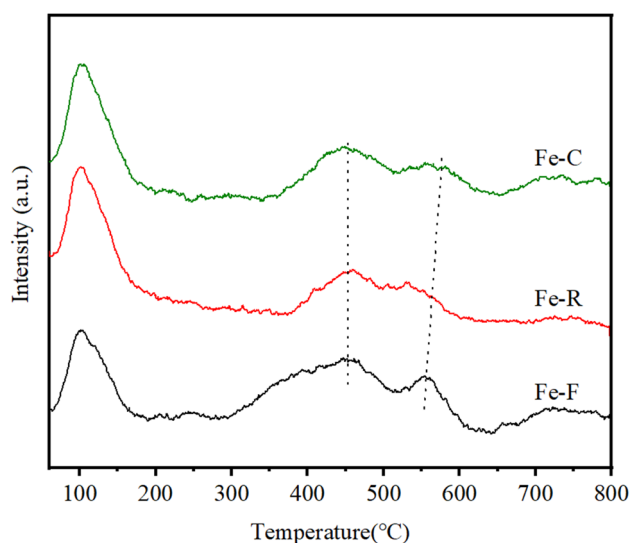
Fig. 4 CO-TPD patterns of the reduced catalysts

to the SEM results, the dispersion of Fe–C nanoparticles formed by concurrent precipitation is significantly better than that of Fe–F nanoparticles formed by forward precipitation. The higher dispersion facilitates the distribution of the active phase, thus improving the FTS activity. Additionally, the reason for the low CO conversion of Fe–F catalysts may be related to the poor reduction ability to form iron carbides, which is thought to be the active phase in FTS [21–23]. The characterization results of CO-TPD mentioned above demonstrate that concurrent precipitation and reverse precipitation promote CO dissociative adsorption compared to forward precipitation, thus increasing CO conversion.

Fe–F catalyst formed by forward precipitation exhibits the lowest CH_4 selectivity (27.4%), the highest $C_2^=$–$C_4^=$ selectivity (28.8%) and C_5^+ selectivity (35.6%) in the hydrocarbon distribution. However, combined with the CO conversion, Fe–C and Fe–R catalysts display the high production of light olefins 303.5 g/(h kg_{Cat}) and 305.3 g/(h kg_{Cat}), respectively.

3.2 Effect of Iron Precursors on Catalysts

The textural properties of precipitated iron-based catalysts with different iron precursors [$Fe(NO_3)_3$, $Fe_2(SO_4)_3$, and $FeCl_3$] are shown in Table 3. Based on the ICP-AES results, the residual Na^+ contents of these three samples are similar (0.15–0.20 wt%). As can be seen from Table 3, Fe–N catalyst has the largest BET specific surface area (31.2 m^2/g) compared to Fe–S and Fe–Cl catalysts [24]. The Fe–S and Fe–Cl catalysts have similar BET specific surface areas of 26.4 m^2/g and 26.2 m^2/g, respectively. Sulfate enters the catalyst pores during the catalyst preparation process and partially clogs the catalyst pores, which leads to a decrease in BET specific surface area [25]. Furthermore, Fe–S catalyst has the largest pore volume (0.30 cm^3/g) and average pore size (33.0 nm) compared to Fe–N and Fe–Cl catalysts.

The XRD patterns of precipitated iron-based catalysts with different iron precursors are shown in Fig. 5. According to JCPDS#87-1164, all three catalysts show the same α-Fe_2O_3 characteristic diffraction peaks at the same locations. Based on the XRD full spectrum, the average crystallite size of α-Fe_2O_3 is calculated using the Scherrer equation, and the results are shown in Table 3. All three catalysts show similar average crystallite size.

The H_2-TPR profiles of precipitated iron-based catalysts with different iron precursors are shown in Fig. 6. The phase transition of iron oxide is similar to Sect. 3.1. It can be seen from Fig. 6 that the precipitated iron catalysts are easily reduced in the order of Fe–Cl > Fe–S > Fe–N, because when $Fe_2(SO_4)_3$ is used as the iron precursor to prepare the catalyst, a small amount of sulfate radical will remain on the catalyst surface, and the presence of sulfur

Table 3 Ar-physisorption results of the fresh catalysts

Catalyst	Na^+ (wt%)[a]	S_{BET} (m^2/g)	V_P (cm^3/g)	D_P (nm)	d_{Fe2O3}[b] (nm)
Fe–N	0.20	31.2	0.25	22.2	19.8
Fe–S	0.15	26.4	0.30	33.0	20.1
Fe–Cl	0.16	26.2	0.24	26.2	19.5

[a]Determined by ICP-AES

[b]Calculated by Scherrer equation according to XRD

Table 2 Activity and selectivity of the catalysts

Catalyst	X_{CO} (%)	S_{CO2} (%)	Distribution of hydrocarbons (%)				O/P[a]	Y ($C_2^=$–$C_4^=$) [g/(h kg_{Cat})]	C balance (%)
			CH_4	C_2^0–C_4^0	$C_2^=$–$C_4^=$	C_5^+			
Fe–F	55.5	42.4	27.4	8.2	28.8	35.6	3.5	189.4	96.4
Fe–C	90.8	39.6	29.2	15.0	26.9	28.9	1.8	303.5	96.8
Fe–R	86.9	40.5	28.5	13.1	28.7	29.7	2.2	305.3	97.1

Reaction condition: T = 320 °C, P = 1.0 MPa, H_2/CO = 2, 12,000 mL/(h g_{Cat}), 24 h

[a]The molar ratio of the alkenes to alkanes in the C_2–C_4 hydrocarbons
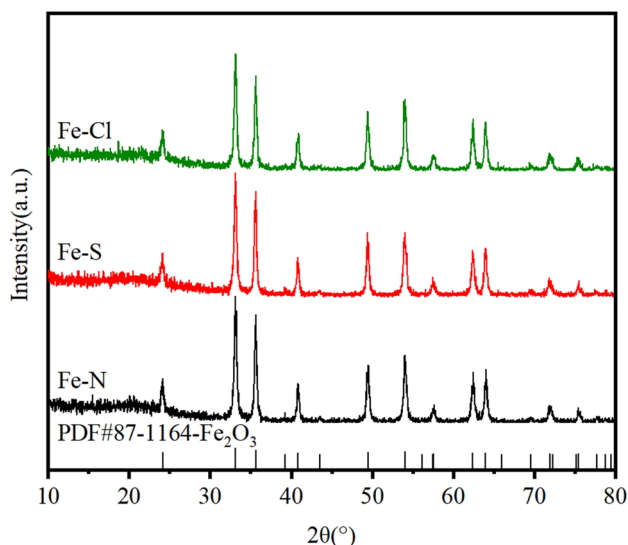
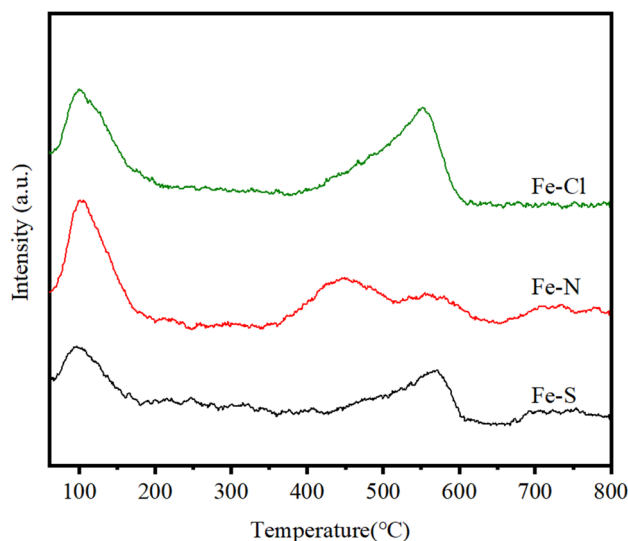**Fig. 5** XRD patterns of fresh catalysts

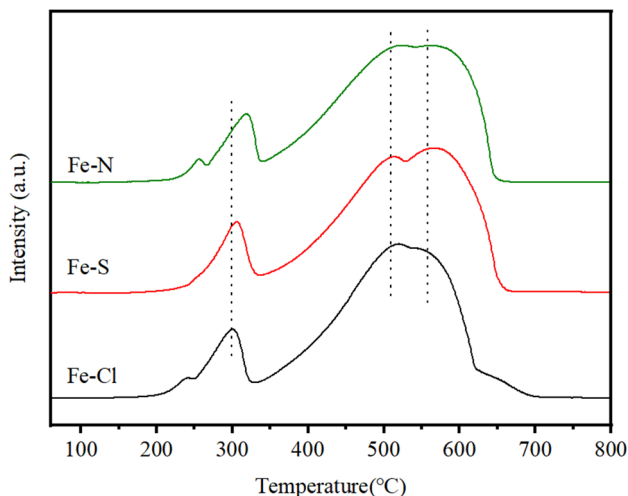**Fig. 7** CO-TPD patterns of the reduced catalysts

Fig. 6 H_2-TPR profiles of the fresh catalysts

element will reduce the catalyst surface alkalinity, thus improving the reduction of Fe–S catalyst [26].

The CO-TPD patterns of the reduced catalysts with different iron precursors are shown in Fig. 7. The types of CO adsorption in different temperature regions are described in Sect. 3.1. On the one hand, the peak areas of CO molecule desorption for Fe–Cl and Fe–N catalysts are significantly larger than that for Fe–S catalyst. On the other hand, the order of CO dissociation desorption peak areas is: Fe–Cl > Fe–N > Fe–S, and the CO dissociation desorption peaks move toward higher temperatures in this order. The results indicate that the dissociative adsorption of CO is best promoted by using $FeCl_3$ as the iron precursor.

The effects of different iron precursors [$Fe(NO_3)_3$, $Fe_2(SO_4)_3$, and $FeCl_3$] on the HTFT synthesis performance are investigated, and the HTFT synthesis activities and hydrocarbon distributions are shown in Table 4. By comparing the CO conversion of catalysts, it can be found that the order of CO conversion is: Fe–Cl (96.6%) > Fe–N (90.8%) > Fe–S (25.9%). According to the H_2-TPR results, Fe–Cl catalyst shows better reduction ability and is more favorable for the formation of active phase iron carbides, which is the active phase during the FTS. Furthermore, the characterization results of CO-TPD mentioned above demonstrate that Fe–Cl and Fe–N catalysts promote CO dissociative adsorption compared to Fe–S catalyst, thus increasing CO conversion. Moreover, the CO conversion of the catalysts prepared with $Fe_2(SO_4)_3$ as the iron precursor is significantly lower than that of the catalysts prepared with $FeCl_3$ and $Fe(NO_3)_3$ as the iron precursor because the presence of sulfur elements inhibits the formation of iron carbide [27].

Fe–Cl catalyst exhibits the lowest CH_4 selectivity (20.2%), the highest $C_2^=-C_4^=$ selectivity (29.1%) and C_5^+ selectivity (42.5%) in the hydrocarbon distribution. In addition, Fe–Cl catalyst displays the highest production of light olefins 372.4 g/(h kg_{Cat}).

3.3 Effect of Precipitants on Catalysts

The textural properties of precipitated iron-based catalysts with different precipitants (ammonium carbonate, sodium carbonate, ammonia solution, sodium hydroxide, and potassium hydroxide) are shown in Table 5. Based on the ICP-AES results, the residual Na^+ contents of Fe-SC and Fe-SH catalysts prepared with sodium carbonate and sodium hydroxide as precipitants are below the lower limit

Table 4 Activity and selectivity of the catalysts

Catalyst	X_{CO} (%)	S_{CO2} (%)	Distribution of hydrocarbons (%)				O/P	Y ($C_2^==C_4^=$) [g/(h kg$_{Cat}$)]
			CH_4	C_2^0–C_4^0	$C_2^=$–$C_4^=$	C_5^+		
Fe–Cl	96.6	35.6	20.2	8.2	29.1	42.5	3.5	372.4
Fe–N	90.8	39.6	29.2	15.0	26.9	28.9	1.8	303.5
Fe–S	25.9	37.0	25.3	6.6	27.8	40.3	4.2	93.3

Reaction condition: T = 320 °C, P = 1.0 MPa, H_2/CO = 2, 12,000 mL/(h g$_{Cat}$), 24 h

Table 5 Ar-physisorption results of the fresh catalysts

| Catalyst	Na$^+$/ K$^+$ (wt%)[a]	S_{BET} (m^2/g)	V_P (cm^3/g)	D_P (nm)	d_{Fe2O3}[b] (nm)
Fe-AC	–	25.1	0.23	24.0	19.4
Fe-SC	< 0.01	27.5	0.25	25.4	18.8
Fe-AH	–	20.1	0.16	21.7	22.2
Fe-SH	< 0.01	22.6	0.31	35.1	23.6
Fe-PH	0.09	21.4	0.17	21.3	23.7

[a]Determined by ICP-AES

[b]Calculated by Scherrer equation according to XRD

of detection (‹ 0.01 wt%), indicating that the residual Na$^+$ is completely washed. And Fe-PH catalysts prepared with potassium hydroxide as precipitant have been washed several times with a residual K content of 0.09 wt%. It can be seen from Table 5 that Fe-AC and Fe-SC catalysts prepared with ammonium carbonate and sodium carbonate as precipitants have a larger specific surface area compared to those prepared with ammonia or hydroxide as precipitants. This may be caused by the formation of CO_2 during the precipitation process, which generates voids in the catalyst structure as CO_2 leaves the catalyst slurry during catalyst preparation, resulting in a catalyst with high porosity and BET specific surface area [7]. Additionally, Fe-SH catalyst has the largest pore volume (0.31 cm^3/g) and average pore size (35.1 nm), followed by Fe-AC and Fe-SC, and finally by Fe-AH and Fe-PH.

The XRD patterns of precipitated iron-based catalysts with different precipitants are shown in Fig. 8. According to JCPDS#87-1164, all three catalysts show the same α-Fe_2O_3 characteristic diffraction peaks at the same locations. Based on the XRD full spectrum, the average crystallite size of α-Fe_2O_3 is calculated using the Scherrer equation, and the results are shown in Table 5. It can be seen from Table 5 that Fe-AC and Fe-SC catalysts prepared with ammonium carbonate and sodium carbonate as precipitants show smaller average crystallite size, which may be due to the formation of CO_2 during precipitation of carbonates, which inhibits the crystal nuclei growth [28].

The H_2-TPR profiles of precipitated iron-based catalysts with different precipitants are shown in Fig. 9. The phase transition of iron oxide is similar to Sect. 3.1. It can be seen
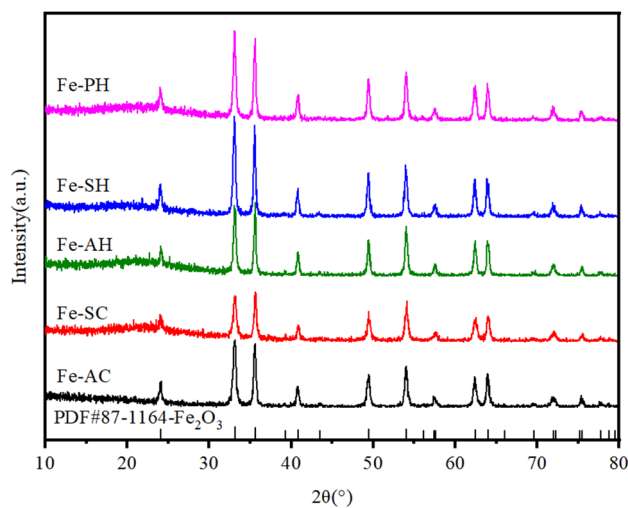
Fig. 8 XRD patterns of fresh catalysts
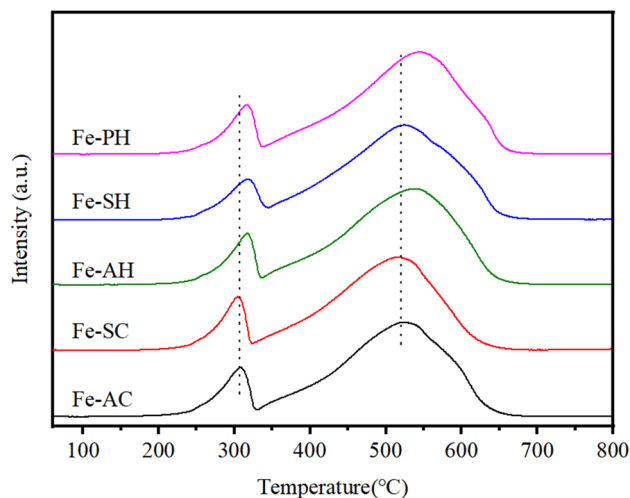
Fig. 9 H_2-TPR profiles of the fresh catalysts

from Fig. 9 that the precipitated iron catalysts are easily reduced in the order of Fe-AC > Fe-SC > Fe-SH > Fe-AH > Fe-PH. The residual K$^+$ on the catalyst surface contributes to the poor reduction ability of Fe-PH catalyst [29, 30].

The effects of different precipitants (ammonium carbonate, sodium carbonate, ammonia solution, sodium hydroxide,

Table 6 Activity and selectivity of the catalysts

Catalyst	X_{CO} (%)	S_{CO2} (%)	Distribution of hydrocarbons (%)				O/P	Y ($C_2^=$–$C_4^=$) [g/(h kg$_{Cat}$)]
			CH_4	C_2^0–C_4^0	$C_2^=$–$C_4^=$	C_5^+		
Fe-AC	38.3	30.6	37.7	14.2	29.5	18.5	2.1	161.3
Fe-SC	27.9	28.6	40.3	16.9	26.3	16.4	1.6	107.8
Fe-AH	28.6	27.4	38.4	13.9	30.0	17.7	2.2	128.1
Fe-SH	11.1	33.2	46.1	9.3	23.8	20.8	2.6	36.3
Fe-PH	34.8	38.1	22.6	7.1	26.5	43.7	3.7	117.4

Reaction condition: T = 320 °C, P = 1.0 MPa, H_2/CO = 2, 12,000 mL/(h g$_{Cat}$), 24 h

and potassium hydroxide) on the HTFT synthesis performance are investigated, and the HTFT synthesis activities and hydrocarbon distributions are shown in Table 6. By comparing the CO conversion of catalysts, it can be found that the order of CO conversion is: Fe-AC (38.3%) > Fe-PH (34.8%) > Fe-AH (28.6%) > Fe-SC (27.9%) > Fe-SH (11.1%). From the BET results, the Fe-AC catalyst prepared with ammonium carbonate as the precipitant show a large BET specific surface area, which facilitates the distribution of the active phase and thus improves the catalytic activity. Moreover, from the H_2-TPR results, Fe-AC catalyst demonstrates good reduction ability and can be easily carbonized to generate the active phase iron carbide, thus exhibiting high FTS activity.

Fe-PH catalyst exhibits the lowest CH_4 selectivity (20.2%), the highest O/P (3.7) and C_5^+ selectivity (43.7%) in the hydrocarbon distribution. This result may be related to the residual K^+ on the catalyst surface. The unwashed K^+ remaining on the catalyst surface can promote the conversion of CO into heavy hydrocarbons and increase the O/P [6]. In addition, combined with the CO conversion, Fe-AC catalyst displays the highest production of light olefins 161.3 g/(h kg$_{Cat}$).

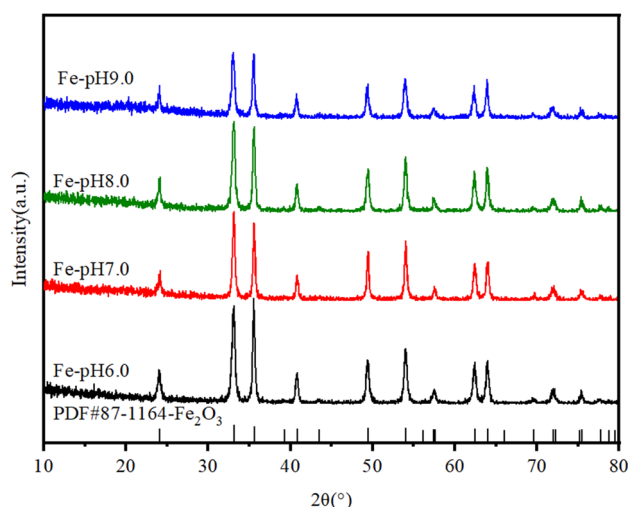## 3.4 Effect of pH Values of Precipitation on Catalysts

The textural properties of precipitated iron-based catalysts with different precipitation pH values (pH = 6.0, 7.0, 8.0, and 9.0) are shown in Table 7. The BET specific surface area was ordered as Fe-pH 6.0 (28.6 m²/g) > Fe-pH 8.0 (25.1 m²/g) > Fe-pH 9.0 (20.7 m²/g) > Fe-pH 7.0 (19.6 m²/g). Additionally, as the precipitation pH values increase from 6.0 to 9.0, pore volume shows a trend of first increasing and then decreasing, with the maximum pore volume of Fe-pH 8.0 catalyst (0.23 cm³/g). And different precipitation pH values have little effect on average pore size [7].

The XRD patterns of precipitated iron-based catalysts with different precipitation pH values are shown in Fig. 10. According to JCPDS#87-1164, all three catalysts show the same α-Fe_2O_3 characteristic diffraction peaks at the same locations. Based on the XRD full spectrum, the average crystallite size of α-Fe_2O_3 is calculated using the

Table 7 Ar-physisorption results of the fresh catalysts

Catalyst	S_{BET} (m²/g)	V_P (cm³/g)	D_P (nm)	d_{Fe2O3}[a] (nm)
Fe-pH6.0	28.6	0.14	24.6	21.2
Fe-pH7.0	19.6	0.17	22.6	23.6
Fe-pH8.0	25.1	0.23	24.0	19.3
Fe-pH9.0	20.7	0.16	24.7	20.5

[a]Calculated by Scherrer equation according to XRD

Fig. 10 XRD patterns of fresh catalysts

Scherrer equation, and the results are shown in Table 7. As the precipitation pH increases from 6.0 to 9.0, the average crystallite size of α-Fe_2O_3 is ordered as follows: Fe-pH 8.0 (19.3 nm) < Fe-pH 9.0 (20.5 nm) < Fe-pH 6.0 (21.2 nm) < Fe-pH 7.0 (23.6 nm).

The H_2-TPR profiles of precipitated iron-based catalysts with different precipitation pH values are shown in Fig. 11. The phase transition of iron oxide is similar to Sect. 3.1. It can be seen from Fig. 11 that the precipitated iron catalysts are easily reduced in the order of Fe-pH 6.0 > Fe-pH 8.0 > Fe-pH 7.0 > Fe-pH 9.0. This result illustrates that precipitation pH values at weakly acidic (pH = 6.0) or weakly
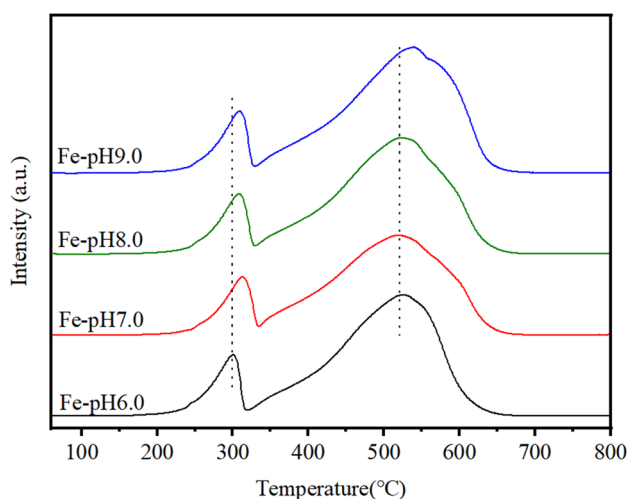
Fig. 11 H₂-TPR profiles of the fresh catalysts

basic (pH = 8.0) facilitate the reduction of Fe nanoparticles, while when the precipitation pH is neutral (pH = 7.0) or strongly basic (pH = 9.0), it inhibits the reduction of catalysts.

The effects of different precipitation pH values (pH = 6.0, 7.0, 8.0, and 9.0) on the HTFT synthesis performance are investigated, and the HTFT synthesis activities and hydrocarbon distributions are shown in Table 8. By comparing the CO conversion of catalysts, it can be found that the order of CO conversion is: Fe-pH 8.0 (38.3%) > Fe-pH 9.0 (36.1%) > Fe-pH 6.0 (35.1%) > Fe-pH 7.0 (28.0%), which is consistent with the ordering of the average crystallite size of catalysts. Combined with XRD, BET and H₂-TPR results, Fe-pH 8.0 catalyst demonstrates small average crystallite size and large BET specific surface area, which promotes the reduction and facilitates the generation of active phase iron carbide in FTS, thus improving the CO conversion. Mirzaei et al. [11] also reported that the catalyst had a high CO conversion when the precipitation pH value was near weakly basic (pH = 8.0).

Different precipitation pH values have little effect on hydrocarbon selectivity in the hydrocarbon distribution. In addition, Fe-pH8.0 catalyst displays the highest production of light olefins 161.3 g/(h kg$_{Cat}$).

3.5 Effect of Temperature of Precipitation on Catalysts

The textural properties of precipitated iron-based catalysts with different temperatures of precipitation (temperature = 25 °C, 45 °C, 65 °C, 75 °C, and 85 °C) are shown in Table 9. The BET specific surface area was ordered as Fe-Tem65 (28.1 m²/g) > Fe-Tem45 (26.2 m²/g) > Fe-Tem75 (25.5 m²/g) > Fe-Tem25 (25.1 m²/g) > Fe-Tem25 (20.5 m²/g). With the increase of the precipitation temperature from 25 to 85 °C, the BET specific surface area of catalysts shows a trend of first increasing and then decreasing. The BET specific surface area reaches the maximum value at the precipitation temperature of 65 °C. Fe-Tem25 and Fe-Tem45 exhibit lower BET specific surface area and smaller average crystallite size. This result indicates that the generation rate of nuclei is higher than the growth rate of crystal at the precipitation temperature below 65 °C, leading to a more aggregation of α-Fe₂O₃ nanoparticles, which results in a lower BET specific surface area [31]. Similarly, the pore volume tends to increase and then decrease as the precipitation temperature increases from 25 to 85 °C. The pore volume of Fe-Tem65 catalyst is the largest at 0.23 cm³/g. The average pore size gradually increases from 24.0 to 32.8 nm with increasing precipitation temperature.

The XRD patterns of precipitated iron-based catalysts with different temperatures of precipitation are shown in Fig. 12. According to JCPDS#87-1164, all three catalysts show the same α-Fe₂O₃ characteristic diffraction peaks at the same locations. Based on the XRD full spectrum, the average crystallite size of α-Fe₂O₃ is calculated using the

Table 9 Ar-physisorption results of the fresh catalysts

Catalyst	S_{BET} (m²/g)	V_P (cm³/g)	D_P (nm)	d_{Fe2O3}[a] (nm)
Fe-Tem25	25.1	0.23	24.0	19.1
Fe-Tem45	26.2	0.27	28.2	19.4
Fe-Tem65	28.1	0.30	29.3	20.0
Fe-Tem75	25.5	0.27	29.3	20.9
Fe-Tem85	20.5	0.24	32.8	23.3

[a]Calculated by Scherrer equation according to XRD

Table 8 Activity and selectivity of the catalysts

Catalyst	X_{CO} (%)	S_{CO2} (%)	Distribution of hydrocarbons (%)				O/P	Y (C₂⁼–C₄⁼) [g/(h kg$_{Cat}$)]
			CH₄	C₂⁰–C₄⁰	C₂⁼–C₄⁼	C₅⁺		
Fe-pH6.0	35.1	29.2	37.8	14.3	29.3	18.6	2.0	149.8
Fe-pH7.0	28.0	26.8	38.4	13.4	30.0	18.2	2.2	126.5
Fe-pH8.0	38.3	30.6	37.7	14.2	29.5	18.5	2.1	161.3
Fe-pH9.0	36.1	29.2	36.8	13.6	30.3	19.3	2.2	159.3

Reaction condition: T = 320 °C, P = 1.0 MPa, H₂/CO = 2, 12,000 mL/(h g$_{Cat}$), 24 h

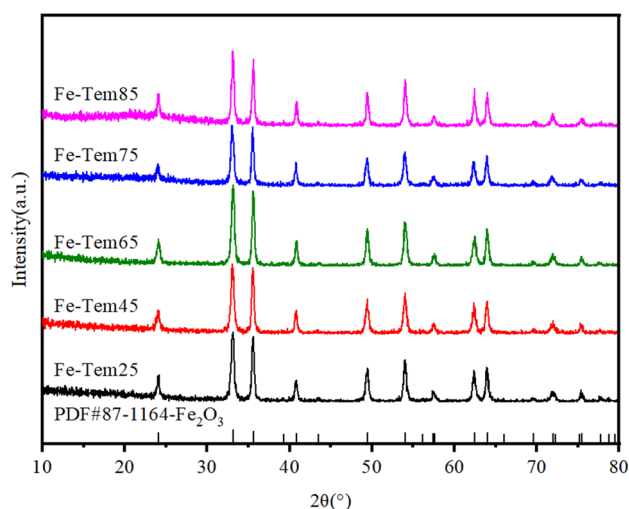**Fig. 12** XRD patterns of fresh catalysts

Fig. 13 H$_2$-TPR profiles of the fresh catalysts

Scherrer equation, and the results are shown in Table 9. As the precipitation pH increases from 6.0 to 9.0, the average crystallite size of α-Fe$_2$O$_3$ is ordered as follows: Fe-Tem25 (19.1 nm) < Fe-Tem45 (19.4 nm) < Fe-Tem65 (20.0 nm) < Fe-Tem75 (20.9 nm) < Fe-Tem85 (23.3 nm). The average crystallite size of the catalysts gradually increases as the precipitation temperature increases from 25 to 85 °C. During the precipitation process, the temperature required for the fastest nuclei generation rate is much lower than that required for the fastest crystal growth rate, so at lower temperatures, the nuclei generation rate is faster than the crystal growth rate, resulting in smaller grains and imperfect crystallization; at slightly higher temperatures, the crystal growth rate is faster than the nuclei generation rate, so the catalyst grains begin to grow and crystallization tends to be perfect [31]. It can be seen that the precipitation temperature can affect the size of iron nanoparticles.

The H$_2$-TPR profiles of precipitated iron-based catalysts with different temperatures of precipitation are shown in Fig. 13. The phase transition of iron oxide is similar to Sect. 3.1. It can be seen from Fig. 13 that the precipitated iron catalysts are easily reduced in the order of Fe-Tem45 > Fe-Tem65 > Fe-Tem25 > Fe-Tem75 > Fe-Tem85. Combining the XRD results, the α-Fe$_2$O$_3$ reduction ability of small grains is stronger compared to the α-Fe$_2$O$_3$ than that of large grains.

The effects of different temperatures of precipitation (temperature = 25 °C, 45 °C, 65 °C, 75 °C, and 85 °C) on the HTFT synthesis performance are investigated, and the HTFT synthesis activities and hydrocarbon distributions are shown in Table 10. By comparing the CO conversion of catalysts, it can be found that the order of CO conversion is: Fe-Tem65 (43.3%) > Fe-Tem75 (43.0%) > Fe-Tem45 (42.4%) > Fe-Tem85 (41.5%) > Fe-Tem25 (38.3%). Combined with XRD,
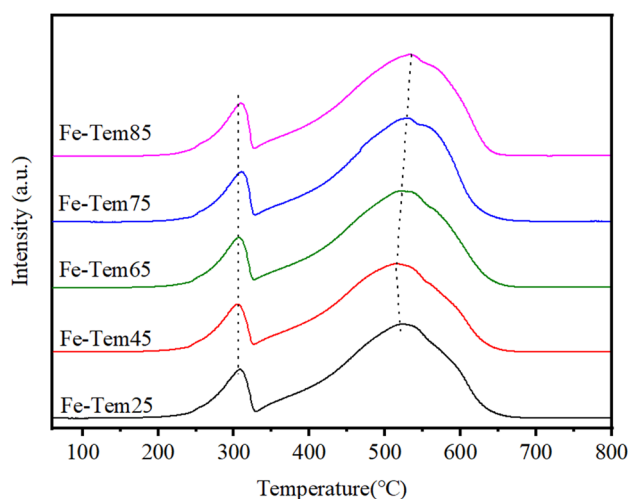
BET, and H$_2$-TPR results, Fe-Tem65 catalyst demonstrates small average crystallite size and large BET specific surface area, which promotes the reduction and facilitates the generation of active phase iron carbide in FTS, thus improving the CO conversion.

As the precipitation temperature increases from 25 to 85 °C, C$_2^=$–C$_4^=$ selectivity slightly decreases from 29.5 to 26.1%, CH$_4$ selectivity first decreases and then increases, while C$_5^+$ selectivity first increases and then decreases. In addition, combined with the CO conversion, Fe-Tem65 catalyst displays the high production of light olefins 172.6 g/(h kg$_{Cat}$).

3.6 Effect of Incorporation Manners of Mn Promoter on Catalysts

The textural properties of precipitated iron-based catalysts with different incorporation manners (precipitation and IWI method) of Mn promoter are shown in Table 11. The BET specific surface area was ordered as Fe (28.1 m^2/g) > FeMn (25.2 m^2/g) > Mn/Fe (20.1 m^2/g).

The introduction of Mn reduces the BET specific surface area of catalysts. And compared with the introduction of Mn by precipitation, the addition of Mn by the IWI method clogs the pore channels of the catalyst, resulting in a significant decrease in BET specific surface area of the Mn/Fe catalyst. In addition, Fe catalyst has the largest average pore size, followed by Mn/Fe catalyst, and the smallest is FeMn catalyst. And different incorporation manners have little effect on average pore size.

The XRD patterns of precipitated iron-based catalysts with different incorporation manners of Mn promoter are shown in Fig. 14. According to JCPDS#87-1164, all three catalysts show the same α-Fe$_2$O$_3$ characteristic diffraction

Table 10 Activity and selectivity of the catalysts

Catalyst	X_{CO} (%)	S_{CO2} (%)	Distribution of hydrocarbons (%)				O/P	Y ($C_2^=$–$C_4^=$) [g/(h kg_{Cat})]
			CH_4	C_2^0–C_4^0	$C_2^=$–$C_4^=$	C_5^+		
Fe-Tem25	38.3	30.6	37.7	14.2	29.5	18.5	2.1	161.3
Fe-Tem45	42.4	32.8	34.0	13.1	29.2	23.8	2.2	171.2
Fe-Tem65	43.3	33.2	32.8	12.6	29.0	25.6	2.3	172.6
Fe-Tem75	43.0	33.2	33.6	13.6	28.4	24.3	2.1	167.8
Fe-Tem85	41.5	36.3	34.8	16.8	26.1	22.3	1.6	141.9

Reaction condition: T = 320 °C, P = 1.0 MPa, H_2/CO = 2, 12,000 mL/(h g_{Cat}), 24 h

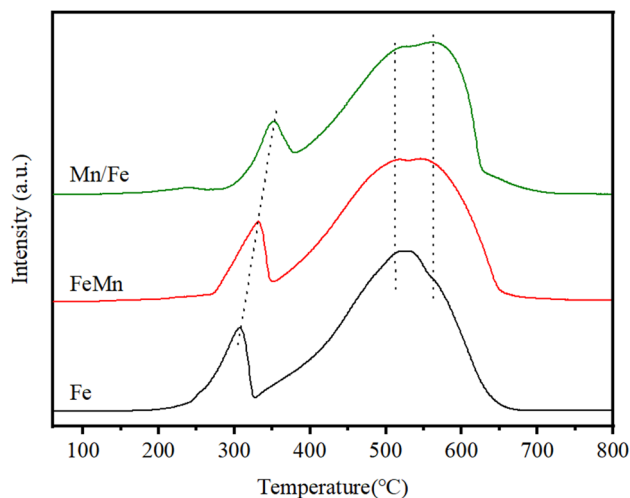**Table 11** Ar-physisorption results of the fresh catalysts

Catalyst	Mn/Fe molar ratioa[a] (%)	S_{BET} (m^2/g)	V_P (cm^3/g)	D_P (nm)	d_{Fe2O3}[b] (nm)
Fe	–	28.1	0.30	29.3	20.0
Mn/Fe	4.9	20.1	0.18	25.8	25.1
FeMn	4.8	25.2	0.18	21.2	25.3

[a]Determined by ICP-AES

[b]Calculated by Scherrer equation according to XRD

Fig. 14 XRD patterns of fresh catalysts
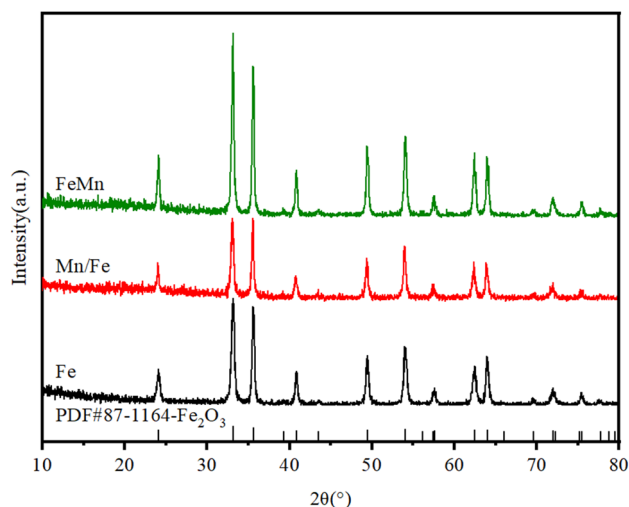
Fig. 15 H_2-TPR profiles of the fresh catalysts

peaks at the same locations. Based on the XRD full spectrum, the average crystallite size of α-Fe_2O_3 is calculated using the Scherrer equation, and the results are shown in Table 11. Obviously, the diffraction peaks of FeMn catalyst exhibit the strongest, indicating that the introduction of Mn facilitates the crystallization of the catalyst. Moreover, FeMn catalyst exhibits the largest average crystallite size, followed by Mn/Fe catalyst, and the smallest is Fe catalyst.

The H_2-TPR profiles of precipitated iron-based catalysts with different incorporation manners of Mn promoter are shown in Fig. 15. The phase transition of iron oxide is similar to Sect. 3.1. It can be seen from Fig. 15 that the

precipitated iron catalysts are easily reduced in the order of Fe > FeMn > Mn/Fe. On the one hand, the introduction of Mn generates FeMn interactions, which inhibits the reduction of α-Fe_2O_3. On the other hand, the introduction of Mn by the IWI method leads to the presence of most MnO_x on the surface of the catalyst, which blocks the pore channel of Mn/Fe catalyst and makes Mn/Fe catalyst reduction poor, while the introduction of Mn by precipitation can promote the dispersion of α-Fe_2O_3 and make FeMn catalyst reduction better.

The CO-TPD patterns of the reduced catalysts with different incorporation manners of Mn promoter are shown in Fig. 16. The types of CO adsorption in different temperature regions are described in Sect. 3.1. On the one hand, The Fe-based catalyst without Mn promoter has only one low temperature desorption peak located at 100 °C, which can be attributed to molecular CO adsorption. This result illustrates the weak CO dissociation adsorption capacity of the pure Fe catalyst without a promoter. When the Mn promoter is introduced, the peak area of the molecular CO desorption peak increases and shifts toward higher temperatures. Moreover, a clear high-temperature desorption peak appears near 400 °C, which can be attributed to CO dissociative adsorption. This
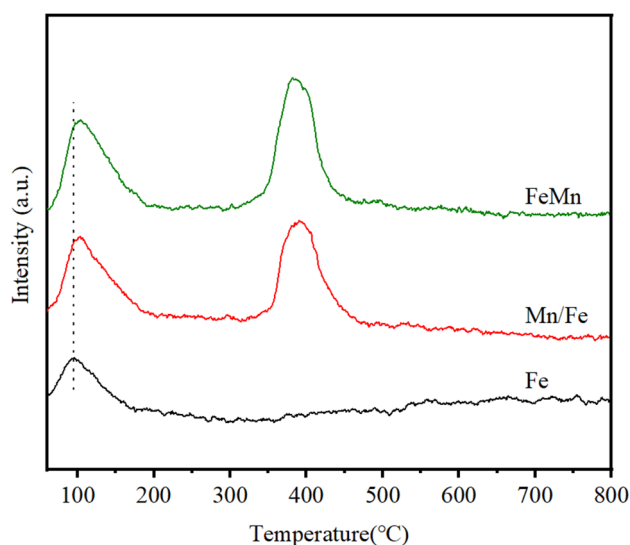
Fig. 16 CO-TPD patterns of the reduced catalysts

result indicates that the addition of Mn can promote CO molecular adsorption and CO dissociative adsorption. On the other hand, the desorption temperature and peak area of the first desorption peak for FeMn and Mn/Fe catalysts are not significantly different, indicating that different incorporation manners of Mn promoter can not significantly affect the CO molecular adsorption. However, the peak area of the second desorption peak of the FeMn catalyst is stronger than that of the Mn/Fe catalyst, indicating that the introduction of Mn into the catalyst in a precipitation manner can promote CO dissociative adsorption.

The effects of different incorporation manners (precipitation and IWI method) of Mn promoter on the HTFT synthesis performance are investigated, and the HTFT synthesis activities and hydrocarbon distributions are shown in Table 12. By comparing the CO conversion of catalysts, it can be found that the order of CO conversion is: FeMn (85.9%) > Mn/Fe (81.0%) > Fe (43.3%). The characterization results of CO-TPD mentioned above demonstrate that the introduction of Mn into the catalyst in a precipitation manner can promote CO dissociative adsorption, thus improving the CO conversion. Combined with BET and H_2-TPR results, compared with Mn/Fe catalysts, FeMn catalyst demonstrates large BET specific surface area, which promotes the

reduction and facilitates the generation of active phase iron carbide in FTS, thus enhancing the CO conversion.

Fe catalyst without Mn promoter exhibits the lowest CH_4 selectivity (32.8%), the highest $C_2^=–C_4^=$ selectivity (29.0%) and C_5^+ selectivity (25.6%) in the hydrocarbon distribution. However, combined with the CO conversion, FeMn catalyst displays the highest production of light olefins 284.6 g/(h kg_{Cat}).

4 Conclusions

The effect of preparation conditions on precipitated iron-based catalysts for HTFT of light olefins was discussed. The iron-based catalysts with the optimum catalytic performance were prepared under the following conditions: ammonium carbonate as the precipitant and ferric trichloride as the iron precursor by concurrent precipitation method at pH 8.0 and 65 °C, followed by the introduction of Mn promoter by precipitation method.

According to the SEM results, the dispersion of Fe–C nanoparticles formed by concurrent precipitation is significantly better than that of Fe–F nanoparticles formed by forward precipitation. The higher dispersion facilitates the distribution of the active phase, thus improving the FTS activity. Concurrent precipitation promotes CO dissociative adsorption compared to forward precipitation, thus increasing CO conversion and the production of light olefins. According to the H_2-TPR results, Fe–Cl catalyst shows better reduction ability and is more favorable for the formation of active phase iron carbides. Fe–Cl catalyst promotes CO dissociative adsorption compared to Fe–N and Fe–S catalysts, thus increasing CO conversion and the production of light olefins. From the BET results, the Fe-AC catalyst prepared with ammonium carbonate as the precipitant show a large BET specific surface area, which facilitates the distribution of the active phase and thus improves the catalytic activity. From the H_2-TPR results, Fe-AC catalyst demonstrates good reduction ability and can be easily carbonized to generate the active phase iron carbide, thus exhibiting high FTS activity. Additionally, the effect of pH values and temperature of precipitation on catalysts was investigated. Combined with XRD, BET, and H_2-TPR results, Fe-pH 8.0 and Fe-Tem65 catalyst demonstrate small average crystallite size and large

Table 12 Activity and selectivity of the catalysts

Catalyst	X_{CO} (%)	S_{CO2} (%)	Distribution of hydrocarbons (%)				O/P	Y ($C_2^=–C_4^=$) [g/(h kg_{Cat})]
			CH_4	$C_2^0–C_4^0$	$C_2^=–C_4^=$	C_5^+		
Fe	43.3	33.2	32.8	12.6	29.0	25.6	2.3	172.6
Mn/Fe	81.0	39.9	34.2	21.2	23.6	21.0	1.1	236.3
FeMn	85.9	39.9	36.2	17.5	26.8	19.5	1.5	284.6

Reaction condition: T = 320 °C, P = 1.0 MPa, H_2/CO = 2, 12,000 mL/(h g_{Cat}), 24 h

BET specific surface area, which promotes the reduction and facilitates the generation of active phase iron carbide in FTS, thus improving the CO conversion and the production of light olefins. Finally, the effect of incorporation manners of Mn promoter on catalysts was analyzed. Combined with BET and H_2-TPR results, compared with Mn/Fe catalysts, FeMn catalyst demonstrates large BET specific surface area, which promotes the reduction and facilitates the generation of active phase iron carbide in FTS, thus promoting CO dissociation adsorption, leading to higher conversion of CO and production of light olefins.

Supplementary Information The online version contains supplementary material available at https://doi.org/10.1007/s11244-022-01684-5.

Declarations

Conflict of interest There are no conflicts to declare.

References

1. Davidson AL, Webb PB, Silverwood IP, Lennon D (2020) The application of quasi-elastic neutron scattering to investigate hydrogen diffusion in an iron-based Fischer-Tropsch synthesis catalyst. Top Catal 63(3–4):378–385
2. Liu Y, Deng D, Bao X (2020) Catalysis for selected C1 chemistry. Chem 6(10):2497–2514
3. Galvis HMT, Bitter JH, Khare CB, Ruitenbeek M, Dugulan AI, de Jong KP (2012) Supported iron nanoparticles as catalysts for sustainable production of lower olefins. Science 335(6070):835–838
4. Toncón Leal CF, Amaya Roncancio S, García Blanco AA, Moreno MS, Sapag K (2019) Confined iron nanoparticles on mesoporous ordered silica for Fischer-Tropsch synthesis. Top Catal 62(12–16):1086–1095
5. Xue Y, Liu Z, Zhang Y, Duan S, Chen J (2021) Effect of the valence state of iron in the precursors on the Fischer-Tropsch synthesis performance of an Fe/Fe foam catalyst. Ind Eng Chem Res 60(6):2410–2417
6. Zhao M, Cui Y, Sun J, Zhang Q (2018) Modified iron catalyst for direct synthesis of light olefin from syngas. Catal Today 316:142–148
7. Motjope TR, Dlamini HT, Hearne GR, Coville NJ (2002) Application of in situ Mössbauer spectroscopy to investigate the effect of precipitating agents on precipitated iron Fischer-Tropsch catalysts. Catal Today 71(3):335–341
8. Mai K, Elder T, Groom LH, Spivey JJ (2015) Fe-based Fischer Tropsch synthesis of biomass-derived syngas: effect of synthesis method. Catal Commun 65:76–80
9. Torres Galvis HM, Koeken ACJ, Bitter JH, Davidian T, Ruitenbeek M, Dugulan AI, de Jong KP (2013) Effect of precursor on the catalytic performance of supported iron catalysts for the Fischer-Tropsch synthesis of lower olefins. Catal Today 215:95–102
10. Wei Y, Luo D, Zhang C, Liu J, He Y, Wen X, Yang Y, Li Y (2018) Precursor controlled synthesis of graphene oxide supported iron catalysts for Fischer-Tropsch synthesis. Catal Sci Technol 8(11):2883–2893
11. Mirzaei AA, Vahid S, Feyzi M (2009) Fischer-Tropsch synthesis over iron manganese catalysts: effect of preparation and operating conditions on catalyst performance. Adv Phys Chem. https://doi.org/10.1155/2009/151489
12. Feyzi M, Hassankhani A (2011) Synthesis, characterization and catalytic performance of nanosized iron-cobalt catalysts for light olefins production. J Nat Gas Chem 20(6):677–686
13. Wu X, Ma H, Zhang H, Qian W, Liu D, Sun Q, Ying W (2019) High-temperature Fischer-Tropsch synthesis of light olefins over nano-Fe_3O_4@MnO_2 core–shell catalysts. Ind Eng Chem Res 58(47):21350–21362
14. Thommes M, Kaneko K, Neimark AV, Olivier JP, Rodriguez Reinoso F, Rouquerol J, Sing KSW (2015) Physisorption of gases, with special reference to the evaluation of surface area and pore size distribution (IUPAC Technical Report). Pure Appl Chem 87(9–10):1051–1069
15. Ahn C, Bae JW (2016) Fischer-Tropsch synthesis on the Al_2O_3-modified ordered mesoporous Co_3O_4 with an enhanced catalytic activity and stability. Catal Today 265:27–35
16. Han Z, Qian W, Zhang H, Ma H, Sun Q, Ying W (2020) Effect of rare-earth promoters on precipitated iron-based catalysts for Fischer-Tropsch synthesis. Ind Eng Chem Res 59(33):14598–14605
17. Pendyala VRR, Graham UM, Jacobs G, Hamdeh HH, Davis BH (2014) Fischer-Tropsch synthesis: morphology, phase transformation, and carbon-layer growth of iron-based catalysts. ChemCatChem 6(7):1952–1960
18. Gu M, Dai S, Qiu R, Ford ME, Cao C, Wachs IE, Zhu M (2021) Structure–activity relationships of copper- and potassium-modified iron oxide catalysts during reverse water–gas shift reaction. ACS Catal 11(20):12609–12619
19. Li J, Cheng X, Zhang C, Wang J, Dong W, Yang Y, Li Y (2017) Alkalis in iron-based Fischer-Tropsch synthesis catalysts: distribution, migration and promotion. J Chem Technol Biotechnol 92(6):1472–1480
20. Ma Z, Ma H, Zhang H, Wu X, Qian W, Sun Q, Ying W (2021) Direct conversion of syngas to light olefins through Fischer-Tropsch synthesis over Fe–Zr catalysts modified with sodium. ACS Omega 6(7):4968–4976
21. Chang Q, Zhang C, Liu C, Wei Y, Cheruvathur AV, Dugulan AI, Niemantsverdriet JW, Liu X, He Y, Qing M, Zheng L, Yun Y, Yang Y, Li Y (2018) Relationship between iron carbide phases (ε-Fe_2C, Fe_7C_3, and χ-Fe_5C_2) and catalytic performances of Fe/SiO_2 Fischer-Tropsch catalysts. ACS Catal 8(4):3304–3316
22. Opeyemi Otun K, Yao Y, Liu X, Hildebrandt D (2021) Synthesis, structure, and performance of carbide phases in Fischer-Tropsch synthesis: a critical review. Fuel 296:120689
23. Petersen MA, van Rensburg WJ (2015) CO dissociation at vacancy sites on Hägg iron carbide: direct versus hydrogen-assisted routes investigated with DFT. Top Catal 58(10–11):665–674
24. Hayakawa H, Tanaka H, Fujimoto K (2007) Preparation of a new precipitated iron catalyst for Fischer-Tropsch synthesis. Catal Commun 8(11):1820–1824
25. Mishra T, Parida KM (2006) Effect of sulfate on the surface and catalytic properties of iron–chromium mixed oxide pillared clay. J Colloid Interface Sci 301(2):554–559
26. Li T, Yang Y, Tao Z, Wan H, An X, Zhang C, Xiang H, Li Y (2007) Effect of sulfate on an iron manganese catalyst for Fischer-Tropsch synthesis. J Nat Gas Chem 16(4):354–362
27. Xu J, Chang Z, Zhu K, Weng X, Weng W, Zheng Y, Huang C, Wan H (2016) Effect of sulfur on α-Al_2O_3-supported iron catalyst for Fischer-Tropsch synthesis. Appl Catal A 514:103–113
28. Wu X, Qian W, Ma H, Zhang H, Liu D, Sun Q, Ying W (2019) Li-decorated Fe-Mn nanocatalyst for high-temperature Fischer-Tropsch synthesis of light olefins. Fuel 257:120567

29. Yang S, Chun H, Lee S, Han S, Lee K, Kim Y (2020) Comparative study of olefin production from CO and CO_2 using Na- and K-promoted zinc ferrite. ACS Catal 10(18):10742–10759
30. Yang Y, Xiang H, Xu Y, Bai L, Li Y (2004) Effect of potassium promoter on precipitated iron-manganese catalyst for Fischer-Tropsch synthesis. Appl Catal A 266(2):181–194
31. Liu Y, Chen J, Bao J, Zhang Y (2015) Manganese-modified Fe_3O_4 microsphere catalyst with effective active phase of forming light olefins from syngas. ACS Catal 5(6):3905–3909